

# Hybrid Turbulence Models for Unsteady Flow Simulation

M. Mani\*

*The Boeing Company, St. Louis, Missouri 63166-0516*

Two different hybrid turbulence models, Reynolds-averaged Navier–Stokes and large-eddy simulation, have been used for unsteady-flow prediction. The objective of this paper is to show that the unsteady forcing function has no impact on the final solution with sufficient flowfield grid resolutions. However, it has a profound effect on initiating the starting roll-up of unsteady high shear when the grid resolution is insufficient to capture it. The unsteady forcing function can be eliminated without any significant effect on the final solution. The objectives are validated with a transonic jet flow and the accuracy of the models is demonstrated by comparing the results of a supersonic impinging jet with experimental data.

## Nomenclature

$A$	=	amplitude
$C_B$	=	turbulent coefficient for two-equation models
$C_{des}$	=	turbulent coefficient for one-equation Spalart–Allmaras model
$C_\mu$	=	turbulence model constant
$d$	=	distance between grid points and wall boundary
$dx, dy, dz$	=	grid spacing in three-dimensional coordinate
$dt$	=	time increment
$l_B$	=	turbulent length scale
$l_\omega$	=	turbulent length scale in $k$ – $\omega$ model
$P$	=	periodic forcing function
$P_i$	=	periodic forcing function at a node
$\Delta$	=	maximum directional spacing at a node
$\kappa$	=	turbulent kinetic energy
$\phi$	=	phase angle
$\omega$	=	frequency, Hz, or turbulent dissipation rate
$\omega_B$	=	turbulent dissipation rate at a node

## Introduction

OVER the past three decades, computational fluid dynamics (CFD) has become a design tool for aerospace applications. This is mainly due to increased computer speed, robust and improved algorithms, and more realistic turbulence models. Whereas significant progress has been made in accurate prediction of steady flows, unsteady-flow predictions are too costly to be applicable for most engineering applications. One of the barriers in accurate prediction of unsteady flow has been the cost associated with the appropriate turbulence models such as large-eddy simulation (LES) and direct numerical solution (DNS). There has been some progress in applications of LES to flowfield predictions of a configuration subcomponent. However, DNS and LES turbulence models are not yet affordable for high-Reynolds-number design applications in aerospace for the foreseeable future.<sup>1</sup>

In an attempt to overcome the lack of a computationally achievable turbulence model for accurate prediction of unsteady turbulent flows, several investigators<sup>1–4</sup> have introduced hybrid models, which are a combination of the Reynolds-averaged Navier–Stokes (RANS) and LES approaches. In general, these models use the RANS approach in the boundary region, where the grid spacing is

very small and the aspect ratio is very large, and the LES approach is used away from the boundary, where the grid spacing is moderate and the aspect ratio is close to one. In the next section we will discuss in more detail two models that we are currently pursuing.

We will demonstrate the ability of the hybrid models to describe jet flows at a cost that is consistent with engineering studies. The new models allow us to demonstrate that the low-frequency, large-scale structures play a dominant role in the time-averaged jet solution, and noise prediction. The accuracy of the predictions will be demonstrated for a circular transonic jet and a supersonic impinging jet.

In addition, we will highlight the physical phenomena that dominate the formation and growth of the large-scale unsteady structures. We will show, for instance, that the formation and modeling of physically unstable shear profiles is required, but that the small-scale unsteadiness has relatively small impact. This is demonstrated by computing the large-scale unsteadiness with various levels of fidelity and showing that the resulting flow is independent of the unsteady forcing, provided that the grid is resolved sufficiently to capture the large-scale structures and steep, unstable profiles. This result has broad impact because it implies that the initiation scales do not need to be modeled (with isotropically refined grids) and that the flows can be computed affordably using stretched grids more typical of RANS calculations. The grid is only required to resolve the (steady) unstable shear profile and the large-scale isotropic structures.

## Turbulence Methodology

RANS derivations begin by assuming that only the time average of the flow is important and the impact of all unsteadiness on the average flow is accounted for by the turbulence model terms. The underlying Navier–Stokes equations are averaged over all time scales. The time averaging of nonlinear terms introduces many terms, particularly for compressible flow, that are simplified to additional viscous terms and the addition of turbulent viscosity and thermal conductivity that must be modeled. These models are developed based on the fundamental behavior of turbulence on model problems. However, in many flows of interest, there is unsteadiness that is not associated with turbulence and/or not well modeled by turbulence models developed for boundary layers or shear layers.

The cost of RANS calculations is roughly proportional to the number of grid points used in the calculation, which in turn is proportional to the mean shear. This proportionality results from the effort expended to align the grid with the mean shear, and the ability to use high-aspect-ratio grids. The computational grids tend to be highly stretched and nonisotropic, simultaneously resolving the high gradients in the wall inner layer, the relatively constant freestream, and relatively small gradients normal to the shear layer, all with as few points as possible. The highly nonisotropic nature of the grid, using only enough points to resolve gradients of interest, is what makes RANS analyses affordable for large-scale problems

Presented as Paper 2000-2959 at the Fluid Dynamic Conference, St. Louis, USA, 25 January 2002; received 16 October 2002; revision received 10 February 2003; accepted for publication 26 May 2003. Copyright © 2003 by M. Mani. Published by the American Institute of Aeronautics and Astronautics, Inc., with permission. Copies of this paper may be made for personal or internal use, on condition that the copier pay the \$10.00 per-copy fee to the Copyright Clearance Center, Inc., 222 Rosewood Drive, Danvers, MA 01923; include the code 0021-8669/04 \$10.00 in correspondence with the CCC.

\*Boeing Associate Technical Fellow, P.O. Box 516, MC-111-1240. Associate Fellow AIAA.

and needs to be retained for affordable structured and unstructured grid schemes. For more on the RANS model see Ref. 5.

LES methods are also derived from the underlying Navier–Stokes equations. However, instead of averaging over all time scales, LES is a space-averaged model that assumes that only the subgrid-scale (SGS) turbulent phenomena are to be modeled. All other scales are to be resolved in time and space and predicted by the numerics. The impact of the unresolved turbulent phenomena on the Navier–Stokes equations is derived using a spatial filter scaled to the local grid size. This procedure again results in additional viscous terms and the introduction of effective turbulent viscosity and thermal conductivity that must be modeled. This model for the small eddies tends to be less critical to the overall flow characteristics than the RANS models because more of the flow is computed directly.

LES calculations typically use relatively isotropic grids and resolve all scales that do not represent the isotropic turbulence decay. The assumption is that the smallest scales being resolved blend smoothly with the modeled SGS and, thus, should require isotropic grids. LES calculations are inherently time accurate, with the time step limited to that required to resolve the smallest unsteadiness of interest.

The cost of LES calculations tends to be proportional to the fourth power of the highest mean shear. This requirement stems from accuracy requirements for propagating the resolved fluctuations. The grid used for LES calculations tends to be isotropic with very little stretching, and the spatial filter used to model the SGS turbulence assumes isotropic turbulence. Thus, once the volume of interest is defined, the size of the computational grid rises as  $(1/dx)^3$ . In addition, LES calculations are time accurate, and the time step required for time accuracy is proportional to  $dx$ . The subsequent rapid rise of cost as finer scales are resolved currently limits LES calculations to relatively low frequency, large-wavelength phenomena. The resulting grid resolution in turn limits the maximum shear that can be modeled in an LES calculation to levels associated with the unsteady phenomena of interest. Thus, LES calculations often must neglect high mean shear regions (which are responsible for most of the turbulence generation) and often cannot be used for flows of engineering interest.

Hybrid methods are a combination of the RANS and LES turbulence models. It is a single model that, in a highly stretched grid, utilizes the RANS approach and, where the grid is more isothermal, utilizes the LES methods. Alternatively stated, the hybrid method extends the RANS turbulence models to accurately model low-frequency, large-wavelength phenomena by utilizing LES approximations for the resolved unsteadiness. The advantages of such methods include limiting the cost of LES calculations by allowing only resolution of interesting scales, simultaneous modeling of high-shear regions and large-scale unsteadiness, and use of a stretched grid. In this study we employed the one-equation Spalart–Allmaras (SA) model<sup>6</sup> with detached-eddy simulation (DES) and the two-equation shear stress transport (SST)<sup>7</sup> with large-eddy stress balance (LESB).

In the SA model, the wall distance in the destruction term is replaced by  $l_B$ , and in the SST model the length scale is replaced by  $l_B$ , where  $l_B$  is defined as follows:

$$l_B = \min(d, C_B \Delta) \quad (\text{SA})$$

$$l_B = \min(l_\omega, C_B \Delta) \quad (\text{SST})$$

where we have a single model that acts as RANS when  $d$  or  $l_\omega \ll \Delta$  and as a LES model when  $\Delta \ll d$  or  $l_\omega$ . For isotropic grids the variable  $\Delta$  can be calculated as follows:

$$\Delta = (\text{volume})^{1/3} = (1/\text{Jacobian})^{1/3}$$

In the boundary layer where the grid is highly stretched, we assume eddies are roughly isotropic and therefore must be resolved in all three coordinate directions and in time:

$$\Delta = \max(dx, dy, dz) \quad (\text{SA})$$

$$\Delta = \max(dx, dy, dz, u^* dt, \sqrt{k^*} dt) \quad (\text{SST})$$

For two-dimensional flow one should note that the turbulent eddies are isotropic; therefore set  $dz$  to infinity, so  $d$  or  $l_\omega \ll \Delta$ , and the equation reverts to the underlying one- or two-equation model (RANS). The coefficients  $C_{des}$  and  $C_B$  are set by experimenting with homogeneous turbulence and requiring a fair behavior of the spectrum at small scale. Spalart defines “fair” as avoiding the buildup of the high-frequency oscillations without suppressing valuable resolvable eddies. Shur et al.<sup>8</sup> recommend a value of 0.65 for  $C_{des}$ . We have found that these coefficients depend on the applications; a value of 0.1 seems to be appropriate for most transonic and supersonic jet applications.

The aforementioned capabilities have been implemented in the Wind code<sup>9</sup> for this study. The Wind code is an upwind, implicit, finite volume, with multizone capability. The algorithm employed for this study is second-order accurate in physical space and first-order accurate in time. No limiter, such as total variation diminishing, was employed in this study.

## Results

### Transonic Jet

The first case is a transonic jet at  $M = 0.8$ ,  $p = 22.4$  psi, and  $T = 1000$  R. The coflow is at  $M = 0.1$ ,  $p = 14.7$  psi, and  $T = 518.67$  R. A polar grid with three different grid resolutions was generated to investigate the effects of the grid spacing on the jet with the hybrid models. Figures 1a and 1b show the inflow plane

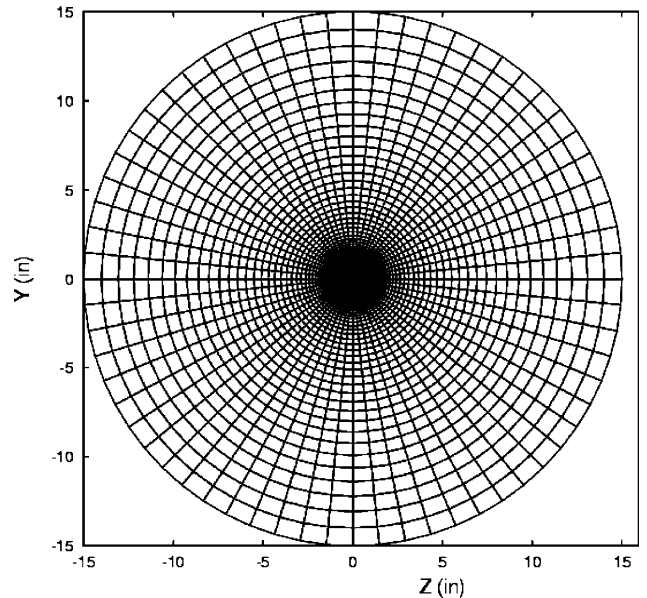


Fig. 1a Inflow plane of the computational domain (coarse grid).

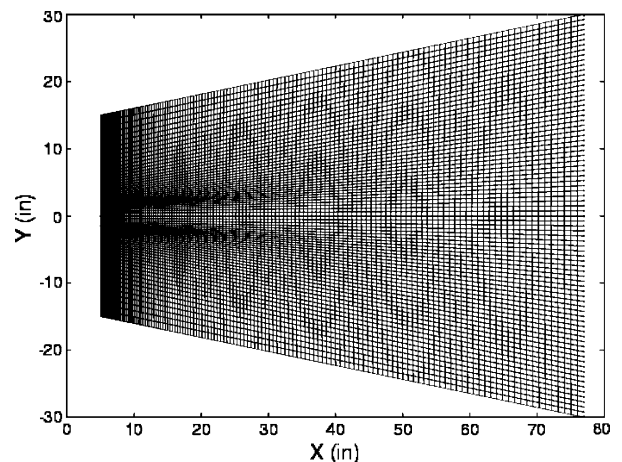
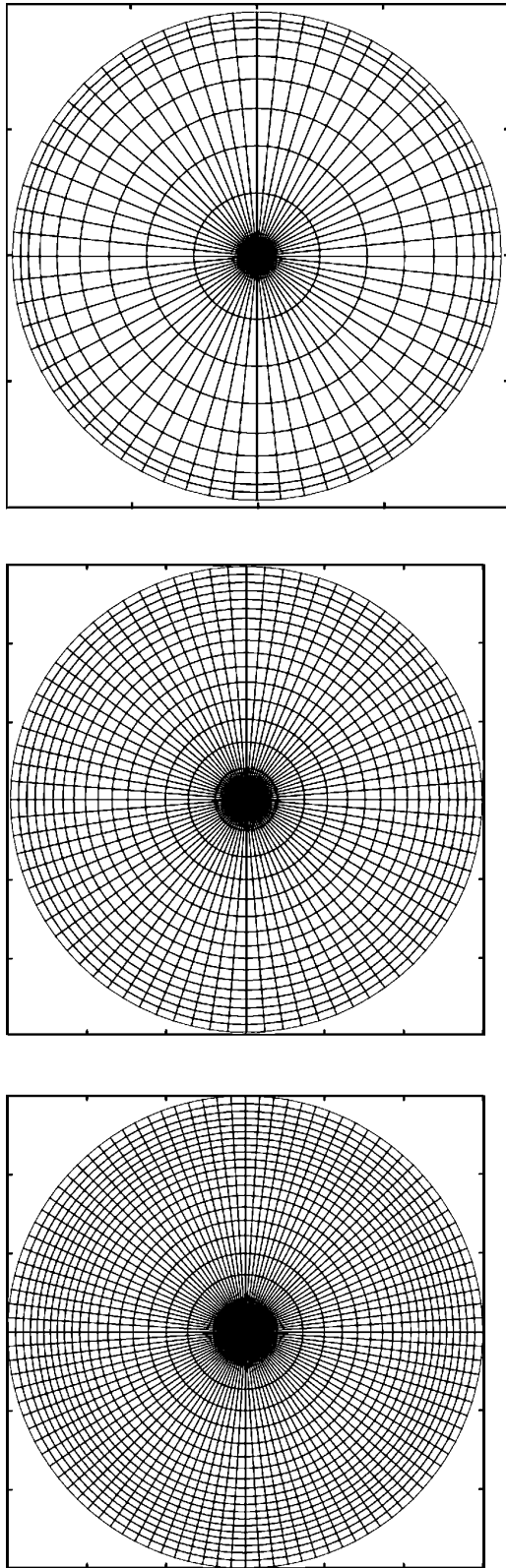
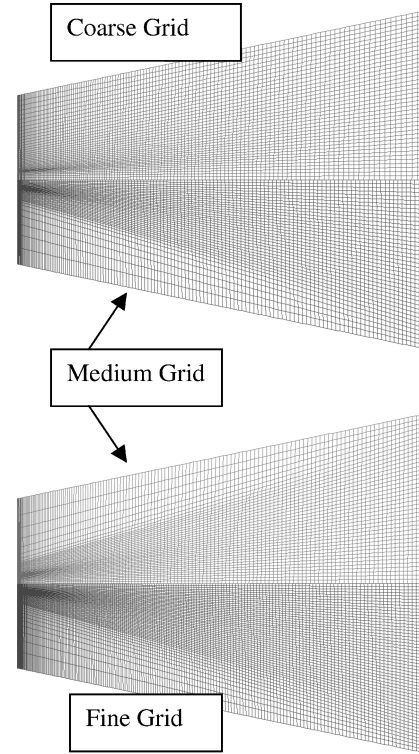


Fig. 1b Cross section of the computational domain (coarse grid).



**Fig. 1c** Grid resolution in jet core.

and longitudinal cross section of the coarse grid, respectively. Because the noise source is located very close to the nozzle exit, most of the axial grid resolution is concentrated near the jet inflow plane where the nozzle exit would be. The grid resolutions for coarse, medium, and fine grids are  $145 \times 41 \times 65$ ,  $145 \times 41 \times 81$ , and  $193 \times 53 \times 105$ , respectively. The number of grid points in the axial and normal directions in the coarse and medium grids is the same. In the medium grid, points are concentrated in the shear layer



**Fig. 1d** Cross sections of the grids.

and near the inflow plane, but the minimum grid spacing in axial and normal directions is the same in both grids. The minimum grid spacing in the fine grid is the same as the coarse and medium, but more points are concentrated in the shear layer and axial directions. The number of grid points in the jet core in the normal directions for the coarse, medium, and fine grids are 9, 17, and 21, respectively. Figure 1c shows the grid resolution in the jet cores and Fig. 1d compares the longitudinal cross section of the three grids.

The results from coarse- and medium grids indicate that the necessary flow features are not being resolved and, therefore, the jet core either does not transition to turbulent or the jet extends much farther than it should before it breaks up. With the coarse grid, the jet core extends farther downstream and the unsteady roll-up decays (Fig. 2a). With the medium and fine grids, the jet transitions to the turbulent flow, the jet core breaks, and the flow becomes fully turbulent (Figs. 2b and 2c). This behavior in the medium and fine grids was somewhat unexpected. We were expecting that the initial roll-up would require a periodic forcing at the inflow or modeling of the nozzle trailing edge. However, it appears that very small numerical disturbances could cause the initial roll-up and, therefore, transition to fully turbulent flows. Figures 2d and 2e show the time-averaged results based on the fine grid over a period of 24 ms. The jet core is much shorter in the time-averaged results (Figs. 2d and 2e) than in the steady-state solution with RANS alone (Fig. 2f).

To investigate the effects of periodic forcing on the solution with different grid resolutions, we introduced a periodic forcing based on the following relation:

$$P_i = P + A^* \cos(\omega t + \phi)$$

where  $A$  is the amplitude,  $\omega$  is the frequency in hertz, and  $\phi$  is the phase angle. Based on the previous computational and experimental results,<sup>10</sup> the peak in dilatation and pressure spectra occurs at about a Strouhal number of 0.25–0.3. Based on this, a periodic forcing at the inflow with 0.1 amplitude and 1400-Hz frequency was introduced. Figure 3a shows the magnitude of vorticity at 10 ms without any inflow forcing function, and Fig. 3b shows the results with the periodic forcing at the inflow. The solution with the periodic forcing restarted from the previous solution, which had no periodic forcing at the inflow. The roll-up is initiated, but gradually decays after

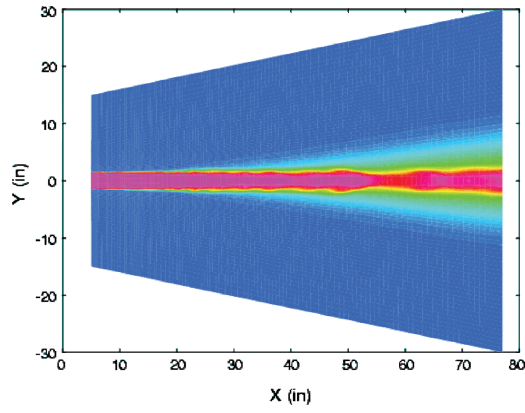


Fig. 2a Coarse grid, entropy at 10 ms.

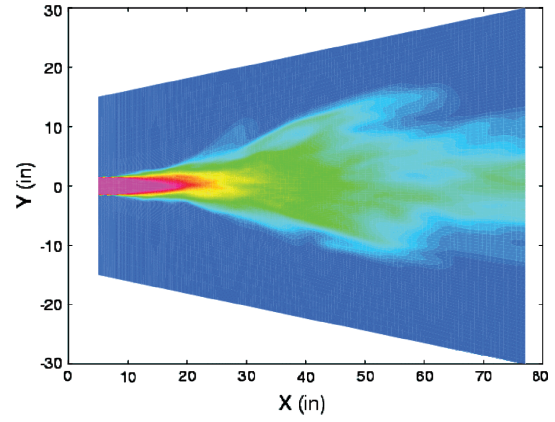


Fig. 2e Fine grid, time-averaged entropy.

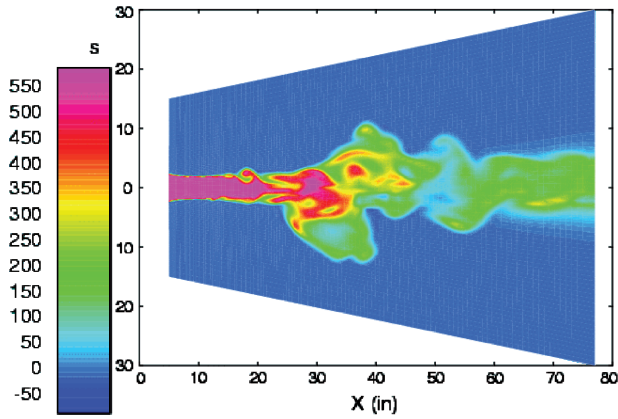


Fig. 2b Medium grid, entropy at 10 ms.

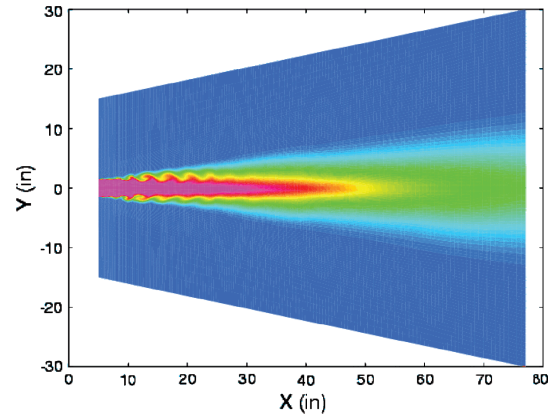


Fig. 2f Fine grid, entropy at steady state.

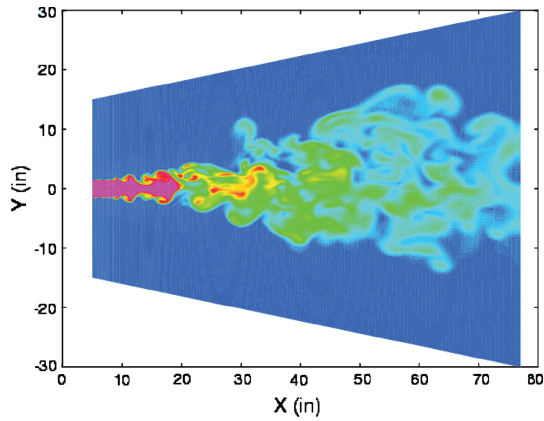


Fig. 2c Fine grid, entropy at 10 ms.

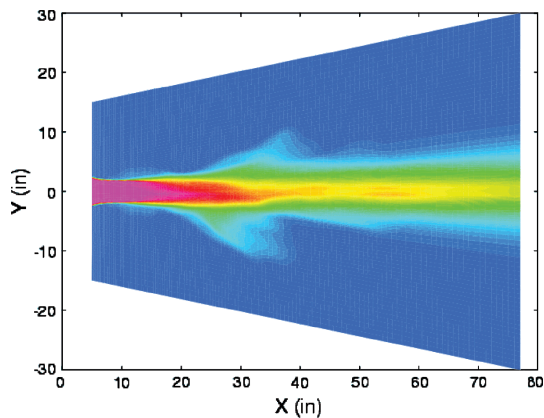


Fig. 2d Medium grid, time-averaged entropy.

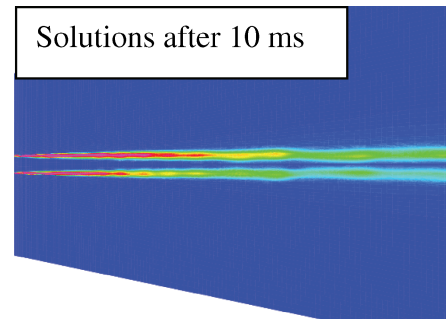


Fig. 3a Coarse grid, no pulse.

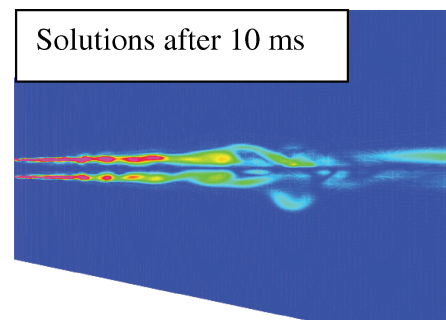


Fig. 3b Coarse grid, with pulse.



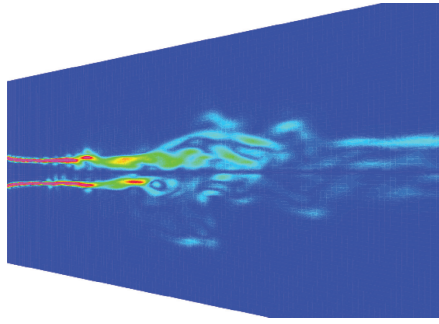


Fig. 4a Medium grid, no pulse.

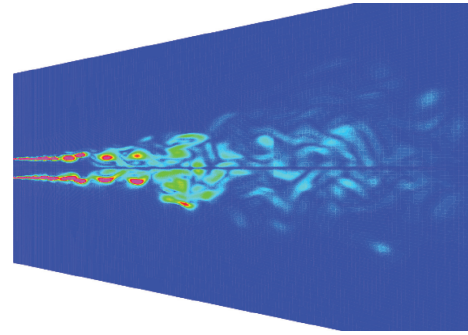


Fig. 5a Fine grid, no pulse.

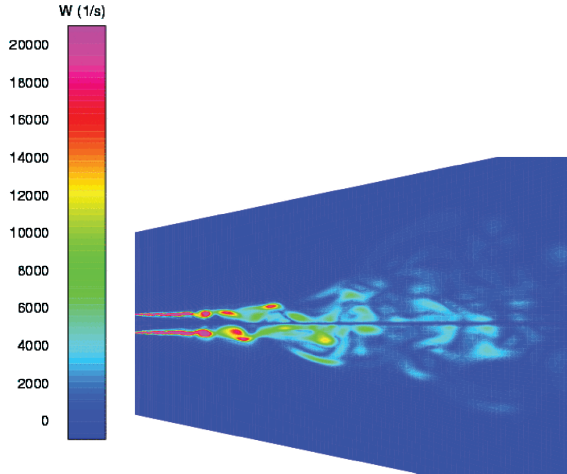


Fig. 4b Medium grid, with pulse.

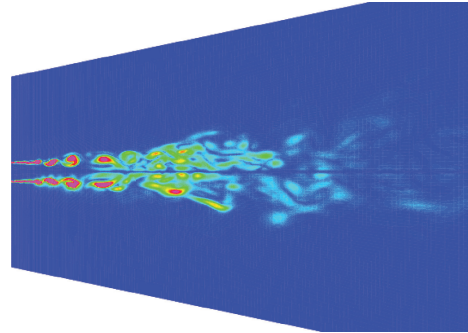


Fig. 5b Fine grid, with pulse.

10 ms. The same thing was performed with the medium and fine grids (Figs. 4 and 5): in both cases, the jets break up and transitions to turbulent flow.

The centerline velocity decay of the time-averaged results without periodic forcing, predicted by the SA-DES, are shown in Fig. 6a. The results are compared to the experimental data of Rodi.<sup>11</sup> The results indicate that the fine-grid velocity decay falls within the experimental data in the first half of the computational domain. The velocity decays too rapidly in the downstream section. To eliminate the effects of the downstream boundary condition, another zone was added to the downstream zone, which extended the computational domain by three times and then the solution continued running for another 24 ms. The results improved slightly, but not enough. The rapid velocity decay might be related to the numerical accuracy. It is recommended that higher-order numerical algorithms be employed for further investigation. In this study we have used a second-order accurate Roe scheme in the physical domain.<sup>12</sup> However, this is not of significant importance because we are interested in the noise prediction, for which the source is farther upstream. The same trend is predicted by the SST-LESb shown in Fig. 6b. This indicates that both models behave very much the same for these types of flows.

To further understand the effects of periodic forcing functions, three solutions were obtained with amplitudes of 0.1, 0.05, and 0.001 and a frequency of 1400 Hz. Three more solutions were obtained with frequencies of 900, 1400, and 1900 Hz, and an amplitude of 0.01. In each series, the solution restarted from the previous solution and ran for 24 ms, which allowed the wave to travel twice the length of the computational domain; at this time the flow is stationary and is no longer changing. Figure 7 depicts the centerline velocity decays for both sets; the computational results are very close to each other and the decay begins at the same location as the data. Farther downstream the computational results are slightly below the data; this is perhaps due to the numerical algorithm, as was pointed out earlier.

To further demonstrate that periodic forcing does not influence the final results, the periodic forcing was removed from the medium grid

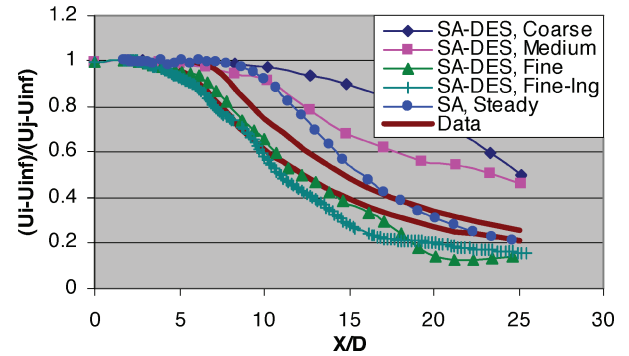


Fig. 6a Centerline velocity decay, SA-DES.

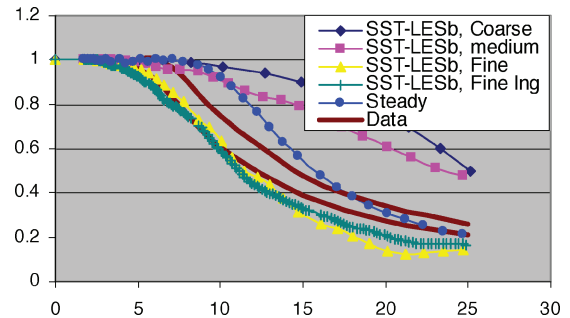


Fig. 6b Centerline velocity decay, SST-LESb.

and the solution was continued for another 24 ms. The centerline velocity decay only changed very slightly toward the outflow boundary (Fig. 8). This is not of any significant importance because the sound source is very close to where centerline decay begins, which in all solutions is identical. It is interesting to note that the results of the centerline decay with medium grid after 24 ms and with removal of the periodic forcing matches the finer grid ( $249 \times 69 \times 137$ ) results very closely. This suggests an enormous cost saving and should be further investigated with other flow conditions.

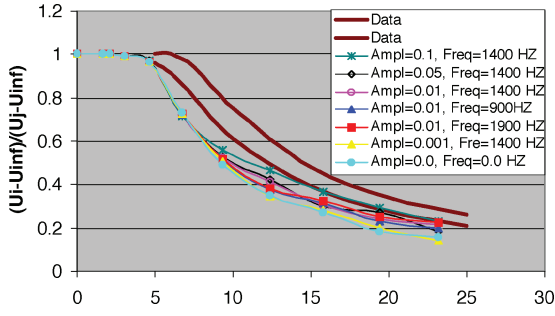


Fig. 7 Centerline velocity decay, SST-LESB.

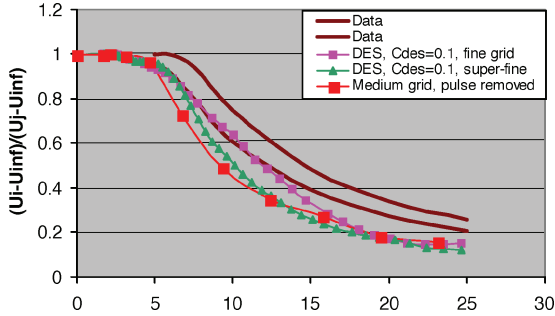


Fig. 8 Centerline velocity decay, SST-LESB.

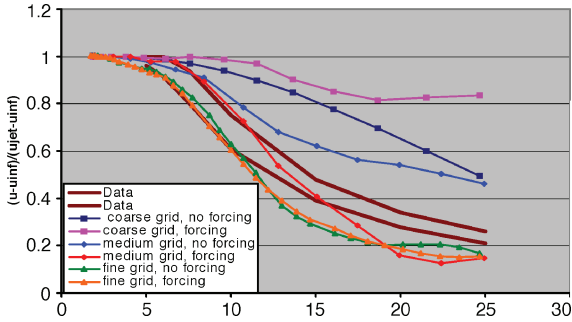


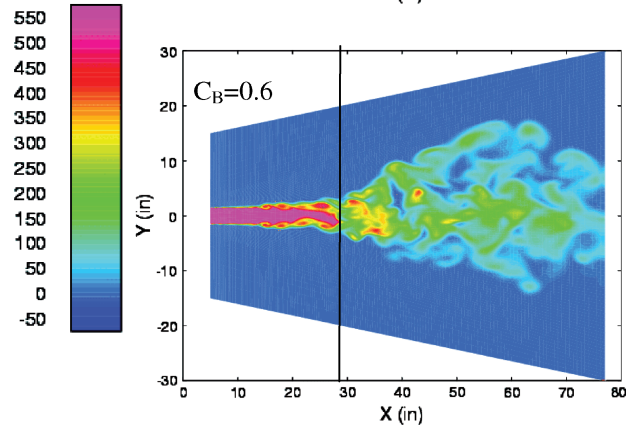
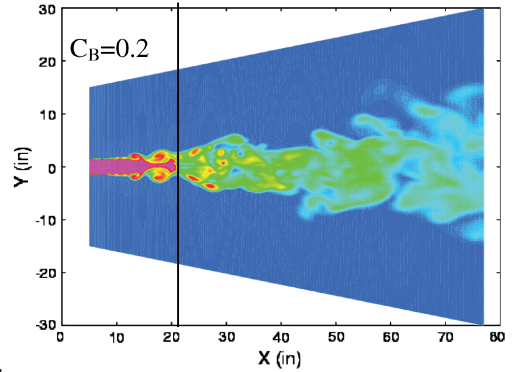
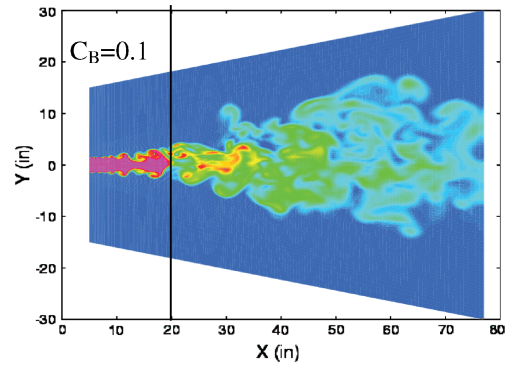
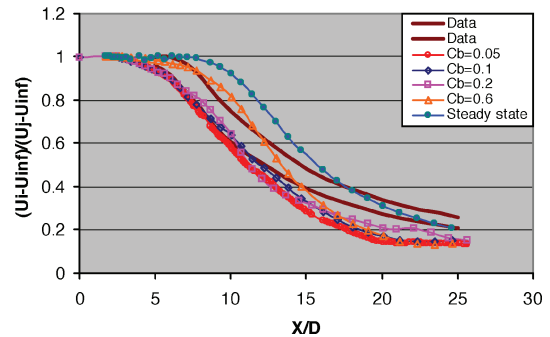
Fig. 9 Centerline velocity decays with and without forcing function.

Figure 9 shows the centerline velocity decay with and without the forcing function for all three grid resolutions. The coarse grid has insufficient resolutions to model the large unsteady flow structures. However, the medium grid has sufficient grid resolution to respond to unsteady impulse and maintain that structure after pulse is turned off. The fine-grid centerline velocity decay demonstrates that the unsteady impulse has no effects on the flow structure when the grid resolution is sufficient to resolve the large unsteady-flow structures.

Both hybrid turbulence models, SA-DES and SST-LESB, have a floating coefficient ( $C_B$ ), which is not universal for all flows. All the preceding solutions were obtained with  $C_B = 0.1$ . This coefficient was chosen based on the centerline velocity decay of the fine-grid solution in comparison with Rodi's data.<sup>11</sup> Figure 10 shows the jet core after 10 ms with  $C_B = 0.1, 0.2$ , and  $0.6$ ; the jet core extends farther as  $C_B$  increases. Figure 11 shows the velocity decay with  $C_B$  for four different  $C_B$  coefficients (0.05, 0.1, 0.2, 0.6). The velocity decay with  $C_B$  of 0.05 and 0.1 are similar and are the closest to the data. When  $C_B$  equals 0.6 the jet core begins to extend toward the steady-state RANS solutions.

#### Supersonic Impinging Jet

The second example represents supersonic impinging jets associated with short takeoff and vertical landing aircraft, which generate a highly oscillatory flow and a strong unsteady load on the aircraft. To investigate this phenomenon, a collaborative experimental and numerical study was performed between the Florida State Univer-

Fig. 10 Entropy contours on the fine grid with three different  $C_B$  coefficients.Fig. 11 Centerline velocity decay with different  $C_B$  coefficients.

sity and the Boeing Company. The experimental setup is shown in Fig. 12. The schematic diagrams of jet interacting with ground are shown in Fig. 13. Where the supersonic flow impinges on the ground the flow splits and forms two opposing recirculation regions. The presence and the reason for the formation of these stagnation bubbles are discussed in Ref. 13. The recirculating regions are shown in Fig. 14 for the Unsteady Reynolds Average Navier-Stokes (URANS) calculations. This recirculation region is stable and steady

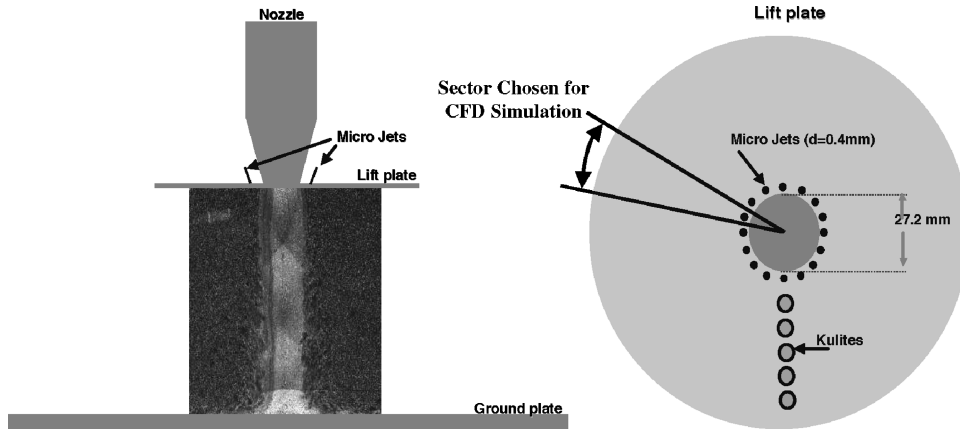


Fig. 12 Flow control experimental setup.

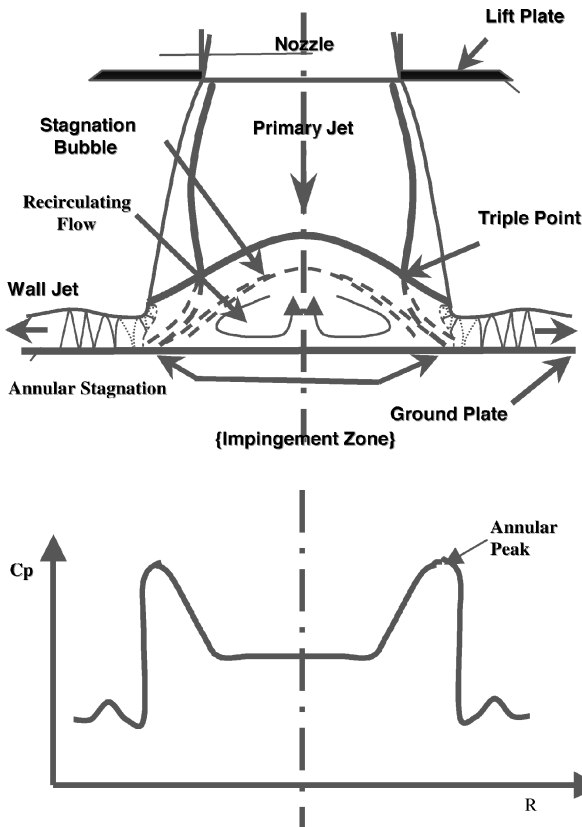


Fig. 13 Schematic and pressure distribution diagrams of stagnation flowfield.

in the URANS calculation but it is unsteady and changes its size in the DES and LESB calculations. The outcome of this investigation<sup>13</sup> was that the unsteady behavior is due to a feedback loop between the fluid and acoustic fields. In that study the numerical investigation was performed using the unsteady RANS approach and the sound prediction on the ground and the lift plate were substantially (about 20 dB) lower than what the experiment predicted.

In the present study two sets of three-dimensional time-accurate computations were made to investigate the effects of turbulence for such flowfields; an unsteady RANS calculation using the standard SA and SST models and similar calculations using the DES and LESB limiter on the turbulent dissipation. All cases produced an unsteady flowfield, and a converged steady state was not possible. The configuration contains a converging-diverging impinging jet with a nozzle pressure ratio equal to 3.7 and a normalized height above the ground plane ( $H/D$ ) of 4.5. The jets were cold and matched

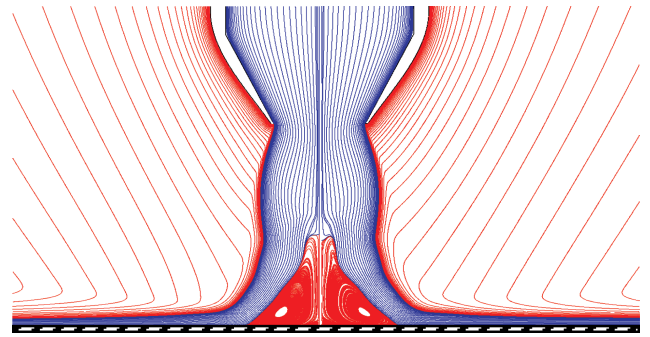
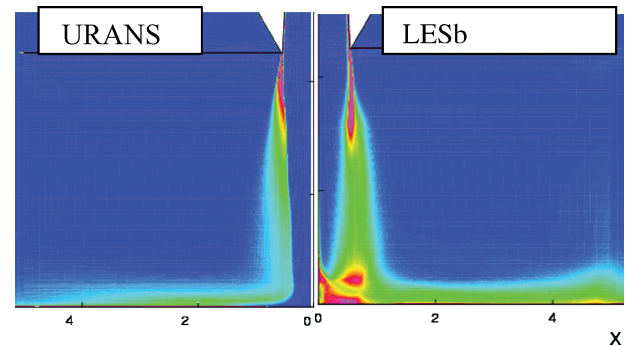


Fig. 14 Computed mean streamline traces.

Fig. 15 Time-averaged specific dissipation rate ( $\omega$ ).

the flow conditions used in the experimental testing ( $M = 0.135$ ,  $P_t = 54.4$  psi,  $T_t = 527.0$  R). Due to computational limitations, a subregion (22.5 deg) of the full 360-deg geometry was used as the domain for the simulations. A periodic boundary condition was assumed for the axisymmetric wedge. The coefficient  $C_B$  of 0.25 was assumed in both turbulence models. Based on the filter implemented in the two-equation model for the LESB,

$$\omega_B = \max(\omega, k^{\frac{1}{2}} / C_\mu C_B \Delta)$$

The dissipation rate  $\omega$  should be similar to the URANS in the boundary-layer region where the grid is highly stretched and it should be greater in the flowfield away from the boundary. This trend can be seen in Fig. 15, where the URANS results are compared with the time-averaged results of the LESB. The instantaneous dissipation rate fluctuations are shown in Fig. 16. The time-averaged Mach contours of LESB and URANS are compared in Fig. 17. The Mach contours intensity is lower in the hybrid model than in the URANS. The hybrid model predicts a larger recirculation near the



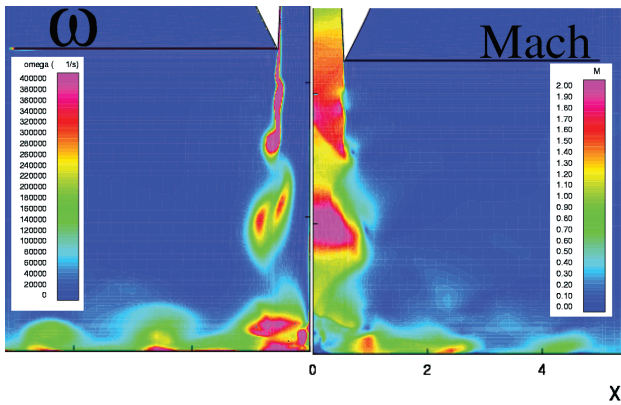


Fig. 16 Instantaneous specific dissipation rate and Mach contours from SST-LESB.

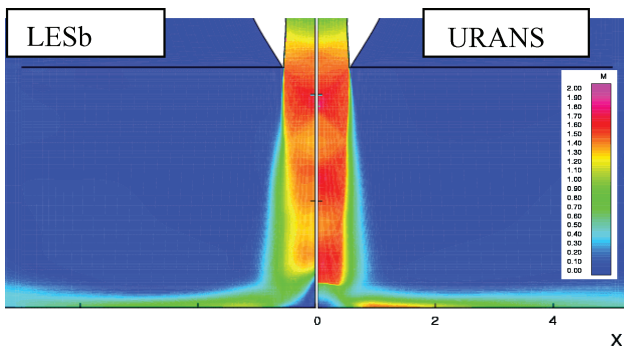


Fig. 17 Mach contours, SST-LESB.

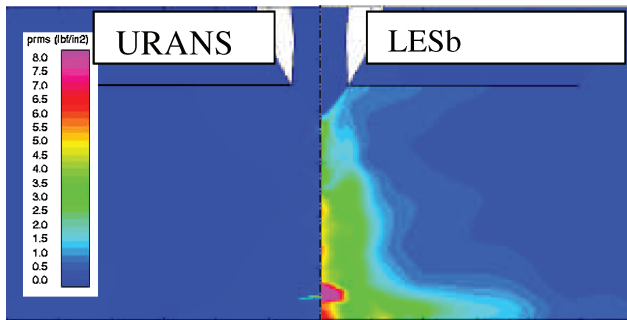


Fig. 18 RMS pressure contours.

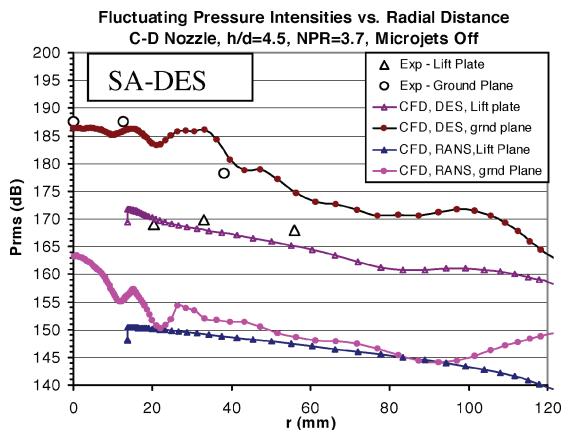


Fig. 19a Radial fluctuating pressure distribution: SA-DES comparison with data and unsteady RANS.

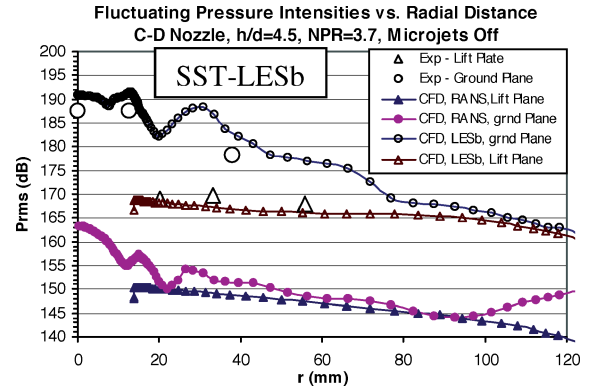


Fig. 19b Radial fluctuating pressure distribution: SST-LESB comparison with data and unsteady RANS.

impinging point than the URANS. The Root Mean Square (RMS) pressure contours on a cross section of the jet with the SST and SST-LESB are shown in Fig. 18. The URANS did not pick up any of the pressure fluctuation except in the Mach disk, whereas the LESB shows substantial pressure fluctuations in the flowfield.

The experimental data for this case include a radial profile of the unsteady pressure fluctuations along the radius of the jet on the ground plane and at the nozzle exit. These data points are compared in Figs. 19a and 19b to the numerical results of URANS (SA and SST) and hybrid (SA-DES and SST-LESB) models, respectively. The URANS results grossly underpredict the pressure fluctuations, whereas the DES and LESB results limit the viscosity substantially to capture the large-scale unsteadiness with remarkable accuracy.

### Summary

The new hybrid RANS/LES turbulence models can accurately predict jet flowfields by resolving only the large-scale structures and using traditional turbulence models only for the dissipation of the fine scales. This allows jet flows to be accurately predicted at a cost consistent with engineering practice. The overhead cost associated with DES and LESB computations is negligible and total computation time is similar to the URANS.

Accurate predictions of jet flows require the resolution of the high-shear unstable profiles. However, highly stretched grids typical of RANS calculations can provide this resolution. The accuracy of the jet flowfield predictions increases from the accuracy typical of RANS calculations to that associated with LES calculations as the isotropic (and time) resolution of the large scales increases. It was shown that engineering accuracy is achieved with isotropic scales that are much larger than that required to resolve the unsteady initiation scales, provided the unstable shear is resolved (on a stretched grid).

The authors suggest that there are additional problems of great engineering interest in which the new hybrid models provide a tool to assess the impact of phenomena of various physical scales. As such, the models open the door to improving the accuracy of flow predictions and applications of CFD to problems previously thought to be beyond the realm of affordability.

### References

- <sup>1</sup>Spalart, P. R., Jou, W. H., Strelets, M., and Allmaras, S. R., "Comments on the Feasibility of LES for Wings, and on a Hybrid RANS/LES Approach," *Advances in DNS/LES*, edited by C. Liu and Z. Liu, Greyden, Columbus, OH.
- <sup>2</sup>Shur, M., Spalart, P. R., Strelets, M., and Travin, A., "Detached-Eddy Simulation of an Airfoil at High Angle of Attack," *4th International Symposium on Engineering Turbulence Modeling and Measurements*, Corsica, 1999.
- <sup>3</sup>Strelets, M., "Detached Eddy Simulation of Massively Separated Flows," AIAA Paper 2001-0879, Jan. 2001.
- <sup>4</sup>Bush, R. H., and Mani, M., "A Two-Equation Large Eddy Stress Model for High Sub-grid Shear," AIAA Paper 2001-2561, June 2001.
- <sup>5</sup>Wilcox, D. C., *Turbulence Modeling for CFD*, 2nd ed., DCW Industries, La Canada, California, 1998.

<sup>6</sup>Spalart, P. R., and Allmaras, S. R., "A One-Equation Turbulence Model for Aerodynamic Flows," AIAA Paper 92-0439, Jan. 1992.

<sup>7</sup>Menter, F. R., "Zonal Two Equation  $k-\omega$  Turbulence Models for Aerodynamic Flows," AIAA Paper 93-2906, July 1993.

<sup>8</sup>Shur, M., Spalart, P. R., Strelets, M., and Travin, A., "Detached-Eddy Simulation of an Airfoil at High Angle of Attack," 4th *International Symposium on Engineering Turbulence Modeling and Measurements*, Corsica, France, 1999.


<sup>9</sup>Bush, R. H., Power, G. D., and Towne, C. E., "Wind: The Production Flow Solver of the NPARC Alliance," AIAA Paper 98-0935, Jan. 1998.

<sup>10</sup>Constantinescu, G. S., and Lele, S. K., "Large Eddy Simulation of a Near Sonic Turbulent Jet and its Radiated Noise," AIAA Paper 2001-0376, Jan. 2001.

<sup>11</sup>Rodi, W., "The Prediction of Free Turbulent Boundary Layer by Use of a Two-Equation Model of Turbulence," Ph.D. Dissertation, Mechanical Engineering Department, Imperial College, London, Dec. 1972.

<sup>12</sup>Cain, A. B., and Bush, R. H., "Numerical Wave Propagation Analysis for Stretched Grids," AIAA Paper 94-0172, Jan. 1994.

<sup>13</sup>Alvi, F. S., and Ladd, J. A., "Experimental and Numerical Investigation of Supersonic Impinging Jets," AIAA Paper 2000-2224, June 2000.



**Introduction to Aircraft Flight Mechanics: Performance, Static Stability, Dynamic Stability, and Classical Feedback Control**

Thomas R. Yechout  
U.S. Air Force Academy

With:  
Steven L. Morris  
David E. Bossert  
Wayne F. Hallgren  
U.S. Air Force Academy

**T**his textbook is based on a successful 15-year approach to teaching aircraft flight mechanics at the U.S. Air Force Academy.

Intended for junior-level students presented with the material for the first time, the book clearly explains all the concepts and derivations of equations for aircraft flight mechanics. The material progresses through aircraft performance, static stability, aircraft dynamic stability, and feedback control. The chapters present real world applications and contain problems. A solutions manual is available from the publisher.

#### Contents:

A Review of Basic Aerodynamics • A Review of Basic Propulsion • Aircraft Performance • Aircraft Equations of Motion • Aircraft Static Stability • Linearizing the Equations of Motion • Aircraft Dynamic Stability • Classical Feedback Control • Aircraft Stability/Control Augmentation • Special Topics • Appendices

AIAA Education Series  
2003, 628 pages, Hardback  
ISBN: 1-56347-577-4  
List Price: \$109.95  
AIAA Member Price: \$79.95



American Institute of  
Aeronautics and Astronautics

Publications Customer Service, P.O. Box 960  
Herndon, VA 20172-0960  
Phone: 800/682-2422; 703/661-1595 • Fax: 703/661-1501  
E-mail: warehouse@aiaa.org • Web: www.aiaa.org